# Lawrence Berkeley National Laboratory
## LBL Publications

**Title**

High-Energy Earth-Abundant Cathodes with Enhanced Cationic/Anionic Redox for Sustainable and Long-Lasting Na-Ion Batteries

**Permalink**

https://escholarship.org/uc/item/5047366c

**Journal**

Advanced Materials, 36(33)

**ISSN**

0935-9648

**Authors**

Zhang, Xu

Zuo, Wenhua

Liu, Shiqi

et al.

**Publication Date**

2024-08-01

**DOI**

10.1002/adma.202310659

**Copyright Information**

Peer reviewed

# High-Energy Earth-Abundant Cathodes with Enhanced Cationic/Anionic Redox for Sustainable and Long-Lasting Na-Ion Batteries

*Xu Zhang, Wenhua Zuo, Shiqi Liu, Chen Zhao, Qingtian Li, Yibo Gao, Xiang Liu, Dongdong Xiao, Inhui Hwang, Yang Ren, Cheng-Jun Sun, Zonghai Chen, Boya Wang, Yunfa Feng, Wanli Yang,\* Gui-Liang Xu,\* Khalil Amine, and Haijun Yu\**

Layered iron/manganese-based oxides are a class of promising cathode materials for sustainable batteries due to their high energy densities and earth abundance. However, the stabilization of cationic and anionic redox reactions in these cathodes during cycling at high voltage remain elusive. Here, an electrochemically/thermally stable P2-$Na_{0.67}Fe_{0.3}Mn_{0.5}Mg_{0.1}Ti_{0.1}O_2$ cathode material with zero critical elements is designed for sodium-ion batteries (NIBs) to realize a highly reversible capacity of $\approx$210 mAh g$^{-1}$ at 20 mA g$^{-1}$ and good cycling stability with a capacity retention of 74% after 300 cycles at 200 mA g$^{-1}$, even when operated with a high charge cut-off voltage of 4.5 V versus sodium metal. Combining a suite of cutting-edge characterizations and computational modeling, it is shown that Mg/Ti co-doping leads to stabilized surface/bulk structure at high voltage and high temperature, and more importantly, enhances cationic/anionic redox reaction reversibility over extended cycles with the suppression of other undesired oxygen activities. This work fundamentally deepens the failure mechanism of Fe/Mn-based layered cathodes and highlights the importance of dopant engineering to achieve high-energy and earth-abundant cathode material for sustainable and long-lasting NIBs.

## 1. Introduction

Large-scale electrochemical-energy-storage systems have the potential to transform the electric grid.[1] Although lithium-ion batteries (LIBs) have played a dominant role in portable electronic devices and electric vehicles, the uneven distribution and limited abundance of lithium resources raise serious concerns on the sustainability and total project cost (200–500 USD kWh$^{-1}$) of LIBs for grid-scale energy storage application.[2] Sodium-ion batteries (NIBs) have been considered as a better candidate due to the high abundance of Na resources and similar working principle to that of LIBs.[3] Recently, commercial NIBs have been developed with energy densities comparable with the commercial LiFePO$_4$-based LIBs. According to Argonne BatPaC simulation, the increase of cathode capacity could greatly lift the cell-specific energy.[4] However, high capacity ($\approx$200 mAh g$^{-1}$) has

X. Zhang, S. Liu, B. Wang, Y. Feng, H. Yu
Institute of Advanced Battery Materials and Devices
College of Materials Science and Engineering
Beijing University of Technology
Beijing 100124, P. R. China
E-mail: hj-yu@bjut.edu.cn

X. Zhang, S. Liu, B. Wang, Y. Feng, H. Yu
Key Laboratory of Advanced Functional Materials
Ministry of Education
Beijing University of Technology
Beijing 100124, P. R. China

W. Zuo, C. Zhao, Y. Gao, X. Liu, Z. Chen, G.-L. Xu, K. Amine
Chemical Sciences and Engineering Division
Argonne National Laboratory
Lemont, Illinois 60439, USA
E-mail: xug@anl.gov

Q. Li, W. Yang
Advanced Light Source
Lawrence Berkeley National Laboratory
Berkeley, CA 94720, USA
E-mail: wlyang@lbl.gov

Q. Li
State Key Laboratory of Functional Materials for Informatics
Shanghai Institute of Microsystem and Information Technology
Chinese Academy of Sciences
865 Changning Road, Shanghai 200050, China

D. Xiao
Beijing National Laboratory for Condensed Matter Physics
Institute of Physics
Chinese Academy of Sciences
Beijing 100190, China

**ADVANCED
SCIENCE NEWS**

www.advancedsciencenews.com

**ADVANCED
MATERIALS**

www.advmat.de

been hardly attained in NIB cathodes under stringent electrochemical/thermo stability requirements. On the other hand, to really enable low-cost and sustainable NIBs, it needs to completely avoid the use of scarce and expensive Co, Ni, and Li that raise serious concerns on the supply chain of raw materials.[5–8] Indeed, despite stable cycle life, many reported sodium cathode materials still contain these elements, which fail to fully fulfil the expected low cost and sustainability of NIBs.[9–12]

To increase the capacity of cathode materials, oxygen anionic redox reactions (ARRs) have been introduced in Li/Na-based layered oxides to provide space for charge compensation beyond the conventional cationic redox reactions (CRRs).[13–15] However, the activation of lattice $O^{2-}$ ions at high voltages often leads to the irreversible release of oxygen, accelerating the structural reconstruction and resulting in the rapid decay of both capacity and voltage.[16–18] Therefore, the harness of oxygen's electrochemistry to realize reversible ARR is critical for achieving high-energy cathode materials, which remains challenging and requires innovative structural design. Compared with Li-ion systems, especially with the Li-rich configuration that seems to be highly irreversible on oxygen behaviors,[19] various Na-ion systems have displayed reversible ARR but during the initial few cycles only.[11,13,14,16,19–35] These works indicate the promising potential of Na-ion electrodes based on ARR, which inspires us to explore optimization strategies that could enable high-voltage operation of Na-ion cathode materials through ARR while maintaining their structural stability over extended cycles.

Mn and Fe are two highly abundant elements in the earth's crust, and thus highly preferable for designing cathode materials for NIBs.[36] However, rapid capacity degradation and severe structural transformation can easily take place in Fe/Mn-based cathode materials at high voltages due to 1) uncontrollable reaction pathways of oxygen ions, 2) detrimental structural degradation associated with Jahn–Teller effect of $Mn^{3+}$ during charge and discharge, 3) the distortion of $FeO_6$ octahedrons and spontaneous migration/trap of $Fe^{3+}$ into alkali metal layer particularly during cycling at high voltage (>4.0 V vs Na/Na$^+$),[35,37–40] and 4) complicated phase transitions with the slide of TM layers.[41] Moreover, the operational safety of batteries becomes also critical for grid-scale energy storage. Thus, the improvement of thermal stability of high-voltage layered oxide cathode materials through rational structure strategies is urgent.[42] However, despite intensive efforts of element substitution,[32] surface coating[43] and electrolyte optimization,[44] to the best of our knowledge, all the merits of a reversible capacity of >200 mAh g$^{-1}$, long cycle life, good thermal stability, and minimum voltage fading during high-voltage operation have not been achieved yet.

In this work, we report a low-cost and environmentally friendly P2-type, Fe/Mn-based material with Mg/Ti co-doping ($Na_{0.67}Fe_{0.3}Mn_{0.5}Mg_{0.1}Ti_{0.1}O_2$, NFMMT) for NIBs. This material delivers a high reversible capacity of over 200 mAh g$^{-1}$ at 20 mA g$^{-1}$ and good cycling performance at high specific currents (74% capacity retention at 200 mA g$^{-1}$ after 300 cy-

cles, 73.1% capacity retention at 400 mA g$^{-1}$ after 200 cycles) within a voltage range of 1.5–4.5 V. To the best of our knowledge, this cycle performance is better than that of most reported sodium layered Fe/Mn-based oxide cathodes with such a high charge cut-off voltage of 4.5 V. The large reversible capacity originates from the combination of transition metal CRR and oxygen ARR, which is clarified by a series of state-of-the-art techniques. Particularly, through a comparative study with the undoped $Na_{0.67}Fe_{0.4}Mn_{0.6}O_2$ (NFM), we show that Mg/Ti co-doping enhances both cationic and anionic redox while, surprisingly, maintaining excellent cycling stability even upon high voltage operations.

## 2. Results and Discussion

### 2.1. Structures of NFM and NFMMT

Both NFM and NFMMT were synthesized by the traditional solid-state reaction. The inductively coupled plasma (ICP) spectroscopy results suggest a composition of $Na_{0.668}Fe_{0.398}Mn_{0.603}O_2$ and $Na_{0.668}Fe_{0.295}Mn_{0.501}Mg_{0.099}Ti_{0.099}O_2$ for NFM and NFMMT, respectively. The structures of these two materials were investigated by synchrotron X-ray diffraction (XRD). As shown in **Figure 1a** (NFMMT) and Figure S1 (Supporting Information) (NFM), both materials exhibit a typical P2-type structure (space group P63/mmc (194)). In this structure, the "ABAB" stacking sequence of oxygen packing constitutes the main frame, TM ions are located in the center of $TMO_6$ octahedrons, and Na$^+$ ions occupy the prismatic sites between TM layers. The Rietveld refinement results (Tables S1,S2, Supporting Information) further indicate both materials has no impurities. The refined lattice parameters of NFM and NFMMT are $a = 2.922(3)$ Å, $c = 11.242(5)$ Å (Table S1, Supporting Information) and $a = 2.917(2)$ Å, $c = 11.239(8)$ Å (Table S2, Supporting Information), respectively. The differences in lattice parameters $a$ and $c$ are smaller than the refinement errors, indicating the nearly unchanged lattice structures after Mg/Ti doping. A structural illustration of NFMMT is provided in Figure 1b, showing the "ABBA" stacking mode and two possible Na$^+$ occupation sites, including Na$_e$ (sharing edges with six $TMO_6$ octahedrons) and Na$_f$ (sharing faces with the upper and lower $TMO_6$ octahedrons). Besides, both NFM and NFMMT can maintain the layered structures even after exposure to air for one month, as indicated by the XRD results in Figures S2,S3 (Supporting Information), which are important for practical applications. Nevertheless, slight peak broadening were observed for NFM instead of NFMMT, indicating the slightly enhanced air stability by Mg/Ti doping.

The morphology of NFMMT was examined by scanning electron microscopy (SEM, Figure S4, Supporting Information), showing the typical particle size of 1–2 µm, a bit smaller that of NFM (Figure S5, Supporting Information). For both materials, all the relevant elements are homogeneously distributed within the particles, as shown by the element maps in Figures S6,S7 (Supporting Information). High-angle annular dark-field (HAADF) and annular bright-field (ABF) scanning transmission electron microscopy (STEM) were further employed to investigate the structures of NFMMT (Figure 1c–f) and NFM (Figure S8, Supporting Information). For NFMMT, TM ions appear as bright

I. Hwang, Y. Ren, C.-J. Sun
X-ray Science Division
Argonne National Laboratory
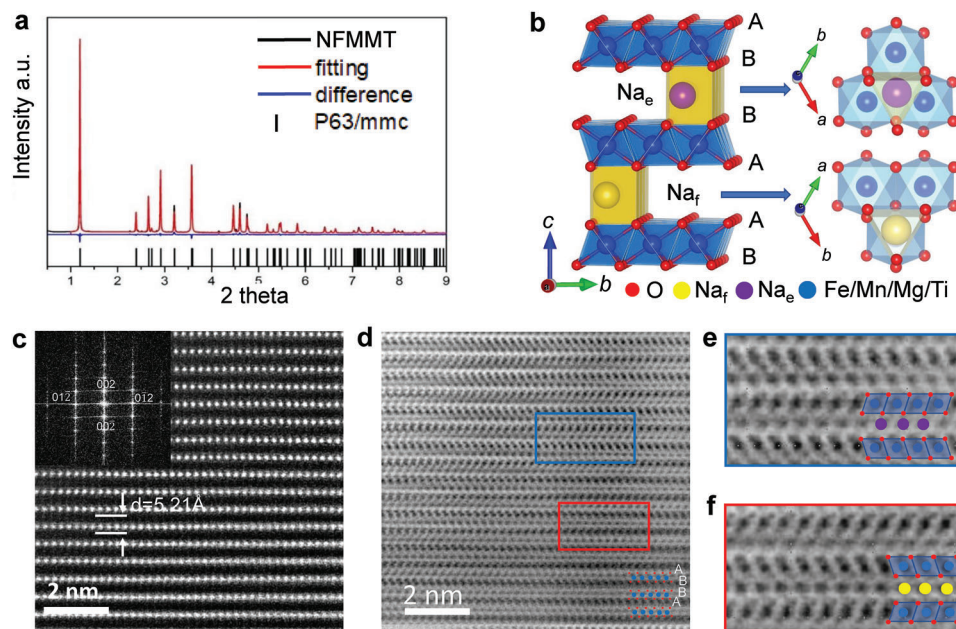9700 South Cass Avenue, Lemont, IL 60439, USA

**ADVANCED
SCIENCE NEWS**

www.advancedsciencenews.com

**ADVANCED
MATERIALS**

www.advmat.de

**Figure 1.** Structural characterizations of NFMMT. a) Synchrotron XRD patterns with structural refinements. b) Structural schematic image with the $Na_e$ and $Na_f$ occupation sites. c) HAADF-STEM image. d) ABF-STEM image. e,f) High-resolution ABF-STEM images of NFMMT showing the $Na_e$ (e) and $Na_f$ (f) occupation sites in the marked regions in (d).

dots in the HAADF image along a straight line, and light element Na and O ions appear as faint dark dots in the ABF image, showing clear "ABBA" stacking sequence in Figure 1e,f. The two $Na^+$ location sites ($Na_e$ and $Na_f$) can also be clearly identified in Figure 1e,f, respectively. Similar structures can be identified for NFM (Figure S8, Supporting Information). Combined with fast Fourier transformation patterns, the STEM results confirm the P2 structure for both NFM and NFMMT, in good agreement with the synchrotron XRD results. In addition, the X-ray photoelectron spectroscopy (XPS) Mg-2p peaks at ≈49.3 eV and the Ti-2p peaks at 457 and 464 eV suggest the valence states of $Mg^{2+}$ and $Ti^{4+}$ at the surface of NFMMT (Figure S9, Supporting Information respectively).

## 2.2. Electrochemical Performance

The electrochemical performances of NFM and NFMMT were investigated in half cells with sodium metal as the anode. Figure S10a (Supporting Information) shows the charge and discharge profiles of NFM, indicating an initial discharge-specific capacity of 186 mAh g$^{-1}$ at 20 mA g$^{-1}$ within a voltage range of 1.5–4.3 V. By further increasing the charge cut-off voltage from 4.3 to 4.5 V, the discharge capacity of NFM increases to 216 mAh g$^{-1}$, with an average operating voltage of 2.6 V (**Figure 2a**; Figure S11, Supporting Information). The increased capacity originates from both the CRR of the Fe element and the ARR of the O element, which will be discussed in the following part.

Figure S10b (Supporting Information) shows that NFMMT delivers an initial discharge capacity of 177 mAh g$^{-1}$ at 20 mA g$^{-1}$ when charged to 4.3 V. When the charge cut-off voltage was increased from 4.3 to 4.5 V, the initial discharge capacity of

NFMMT was increased to 209 mAh g$^{-1}$ at 20 mA g$^{-1}$ (Figure 2b; Figure S11, Supporting Information). Moreover, NFMMT exhibits a longer voltage slope than that of NFM at the high voltage range of 3.6–4.5 V, corresponding to the mixture of both CRR and ARR. Typically, voltage decay is often seen in layered oxides owing to the irreversible structural transformation during the cycling process, which will decrease the specific energy of batteries. Although the doped inactive Mg and Ti slightly reduce the capacity of NFMMT, the discharge voltage can be better maintained in NFMMT than that in NFM (Figure 2c,d), which is beneficial to maintain the specific energy of the battery.

The capacity retention of NFMMT during cycling at high specific currents is significantly improved when compared with that of NFM (Figure 2a,b). As shown in Figure 2e, the reversible capacity of NFM degrades rapidly upon cycling, leading to a capacity retention of only 27.9% (the capacity retention was normalized to the first discharge capacity at 200 mA g$^{-1}$, the same below) after 150 cycles at 200 mA g$^{-1}$. NFM with Ti doping or Mg doping only were also synthesized for comparison (Figure S12, Supporting Information). As shown in Figure 2e, a single dopant cannot effectively suppress the capacity fading during high-voltage cycling, indicating the necessity of co-doping. Indeed, NFMMT with Mg/Ti co-doping exhibits a much better capacity retention of 74% after 300 cycles during charge/discharge at 200 mA g$^{-1}$ within 1.5–4.5 V. Even at a high specific current of 400 mA g$^{-1}$, NFMMT could still deliver a high initial capacity of 167.9 mAh g$^{-1}$ with a capacity retention of 73.1% after 200 cycles (Figure 2f). Moreover, as shown in Table S3 (Supporting Information), NFMMT delivers both higher capacity and better cycle stability, superior to most reported sodium-layered Fe/Mn-based cathodes with a high cut-off voltage of >4.0 V. In addition, NFMMT exhibits a higher capacity retention in the NaClO$_4$ electrolyte than that in a common NP30 electrolyte (1 M NaPF$_6$ in EC: DMC [1:1 v/v], Figure S13,

**ADVANCED
SCIENCE NEWS**

www.advancedsciencenews.com
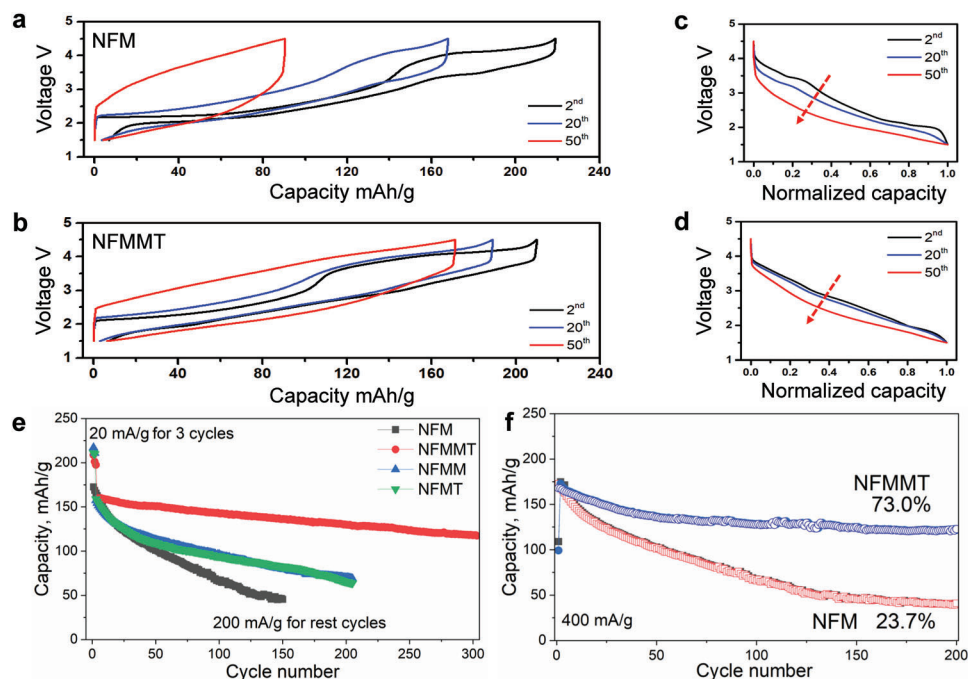
**ADVANCED
MATERIALS**

www.advmat.de

**Figure 2.** Electrochemical performance of NFM, NFMM, NFMT, and NFMMT within 1.5–4.5 V (vs Na/Na⁺). a,b) Charge and discharge profiles of NFM (a) and NFMMT (b) at 20 mA g⁻¹. c,d) Discharge profiles of NFM (c) and NFMMT (d) showing the voltage decay features. e) Discharge capacities of NFM, NFMM, NFMT, and NFMMT cathode during cycling at a specific current of 200 mA g⁻¹ after formation at 20 mA g⁻¹ for 3 cycles. f) Cycling performance of NFM and NFMMT cathode during charge/discharge at a specific current of 400 mA g⁻¹. Hollow and solid symbols represent charge and discharge capacities, respectively.

Supporting Information), which has been ascribed to the synergistic effect between $ClO_4^-$ and $O_2^-$ anions.[21] In addition, after being exposed in air for 15 days, NFMMT still shows much better electrochemical performance than NFM (Figure S14, Supporting Information), further indicating the enhanced air stability by Mg/Ti co-doping. The fabrication of full cells using anodes such as hard carbon is important for the practical application of the developed cathodes. However, P2-type cathodes suffer from inherent sodium deficiency, which requires pre-sodiation for full cells, by strategies such as the electrochemical method, self-sacrificial route, and direct sodium compensation process, which will be further studied at the pouch-cell level.[45]

### 2.3. Electrochemical Structure Evolution

Synchrotron in situ XRD was employed to monitor the structural evolution of the two materials during insertion/extraction of Na⁺. The in situ XRD patterns of NFM in **Figure 3**a and Figure S15 (Supporting Information) show that the P2 (002) peak gradually shifts to lower angles before being charged to 3.6 V, suggesting the expansion of lattice parameter $c$. Meanwhile, the (010), ($\bar{1}$20) and ($\bar{1}$22) peaks gradually shift to higher angles, suggesting the shrinkage of lattice parameter $a$. The intensities of all peaks become lower (voltage < 4.1 V) and then higher (voltage > 4.1 V), indicating the phase transition process of NFM. The (002) peak shifts positively to 1.32° at the end of the charge process, demonstrating the formation of the O2 phase,[46–48] which is related to the slide of TM layers and results in the conversion of Na⁺ oc-

cupation from prismatic to octahedrons sites. An intermediate OP4 phase during the phase transition could be identified,[49,50] with an alternate arrangement of prismatic (P2 phase) and octahedron (O2 phase) Na occupation sites, which is related to the shrinkage of lattice parameter $c$ and weakening of the XRD peaks. Upon the discharge process to 3.2 V, the (002) peak shifts to lower angles and becomes weaker, owing to the expansion of lattice parameter $c$ and phase transition from O2 to P2 through the OP4 phase. When further discharged to 2.0 V, the (002) peak shifts to higher angles, demonstrating the shrinkage of lattice parameter $c$ in the P2 phase. The (010), ($\bar{1}$20), and ($\bar{1}$22) peaks gradually shift back to lower angles, corresponding to the expansion of lattice parameter $a$. Note that new small peaks appear at ≈1.24° and 2.45°, corresponding to the formation of the P'2 phase. Therefore, NFM experiences the complicated P2-OP4-O2-OP4-P2-P'2 phase transition with large volume change during the Na⁺ insertion/extraction process.

As for NFMMT (Figure 3b; Figure S16, Supporting Information), all the XRD peaks exhibit a similar shifting tendency to that of NFM. However, there is no intensity recovery of the weakened XRD peaks, and the (002) peak only shifts to 1.28° at the end of the charge process, demonstrating the P2-to-OP4 phase transition during the extraction of Na⁺. Note that there is no obvious new peak evolution during the charge/discharge process, suggesting a simple P2-OP4-P2 phase transition of NFMMT. As demonstrated in the literature, doping trace amount of Ti will interrupt the in-plane Na-vacancy ordering, weaken the Jahn–Teller effect, minimize the relative dissolution of Mn ions, and thus enhancing the structure stability during the charge/discharge
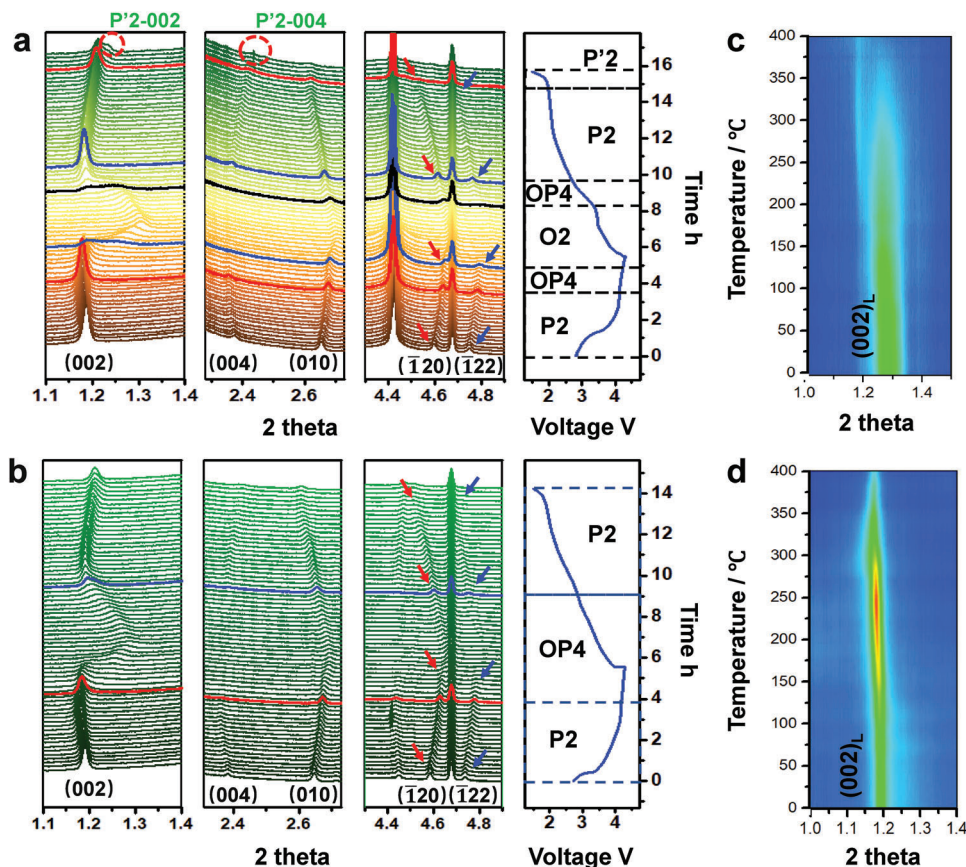
**ADVANCED
SCIENCE NEWS**

www.advancedsciencenews.com

**ADVANCED
MATERIALS**

www.advmat.de

**Figure 3.** Electrochemical and thermal stabilities of NFM and NFMMT. a,b) Synchrotron in situ XRD patterns of NFM (a) and NFMMT (b) in the initial cycle at 20 mA g$^{-1}$ with corresponding initial charge/discharge profiles (right). c,d) The 2D contour plot of HEXRD patterns of (002) peak of NFM (c) and NFMMT (d) as a function of temperature.

process.[51,52] On the other hand, Mg ions in transition-metal oxides will greatly stabilize oxygen by forming strong Mg—O bonds.[19] These effects explain the result that NFM experiences the complicated P2-OP4-O2-OP4-P2-P'2 phase transition, while the Mg/Ti co-doped NFMMT experiences the simple P2-OP4-P2 phase transition.

At the end of the discharge process, peak broadening is observed in both NFM and NFMMT, which may be ascribed to the multiple-phase transition and changes of the lattice.[53] The variations of lattice parameters and cell volume are further calculated by fitting the in situ XRD results. As shown in Figure S17 (Supporting Information), the lattice parameters of NFM experience a series of changes during multiple phase transitions. The volume change is calculated to be 8.21% (based on the equation: volume change = $\frac{V_{max} - V_{min}}{V_{pristine}} \times 100\%$) during the first cycle. For NFMMT, the simple P2-OP4-P2 phase transition is reflected from the lattice parameter changes (Figure S18, Supporting Information) during the first cycle, yielding a calculated cell volume change of 3.9%, which is much smaller than that of NFM.

Synchrotron ex situ XRD measurements of NFM and NFMMT at pristine state, first, second, and 50th cycles were further conducted. All the peaks in the pristine NFM are indexed to the P2 structure (Figure S19, Supporting Information). After the first charge process, the (002) peak shifts to a higher angle with the reduction of intensity, indicating the formation of the O2 structure.

At the first discharged state, NFM exhibits a composite structure characteristic. The (002) peak in Figure S19b (Supporting Information) demonstrates the generation of the P'2 structure, which agrees well with the in situ XRD results. Moreover, NFM in the charged states of the second and 50th cycles exhibit a P2/O2 composite structure. At the discharge state, the content of the P'2 structure gradually increased (Figure S19b, Supporting Information). By contrast, all the structures of NFMMT at the charged states of the first, second, and 50th cycles belong to the OP4 structure without any new peaks (Figure S20, Supporting Information). The discharged states of the first, second, and 50th cycles exhibit a single peak that is similar to the P2 structure but with slight lattice parameter variation. The results further illustrate the better structural stability of NFMMT during the extended charge/discharge process.

In layered oxides, when Mn ions migrate from Mn site (0, 0, 0) to Na$_e$ sites (1/3, 2/3, 3/4), the relative intensities of (012) and (013) peaks become stronger than that of the (002) peak. On the other hand, upon the migration of Mn ions from the Mn site to Na$_f$ sites (0, 0, 1/4), the relative intensities of (004), (100), and (015) peaks become stronger.[54] Thus, peak fitting is further employed to analyze the TM migrations during the charge and discharge process. As shown in Tables S4 and S5 (Supporting Information), all peaks become broader with the increase of cycle numbers, which may be ascribed to the multiple phase

**ADVANCED
SCIENCE NEWS**

www.advancedsciencenews.com

**ADVANCED
MATERIALS**

www.advmat.de

transition and large changes of lattice parameters. The peak intensity ratios (004)/(002) and (013)/(002) become notably enlarged for both materials after the first cycle, suggesting the migration of Mn ions to the Na layer. After 50 cycles, the ratio of peaks (004) and (002) becomes decreased in NFM, which may be due to the dissolution of Mn ions. It is worth noting that the rise of relative intensities of peaks (004) and (013) is smaller in NFMMT than that in NFM, suggesting the Mn migration from the TM layer to the Na layer may be suppressed by the co-doping of Mg and Ti. Moreover, the ICP test suggests that the Mn dissolution of NFMMT (218 ppm) is greatly reduced compared with that of NFM (1308 ppm) during cycling, which is beneficial to the performance of NFMMT.

SEM was also conducted for both NFM and NFMMT after 100 cycles. As shown in Figure S21 (Supporting Information), no crack is observed for both materials at the pristine state. After 100 cycles, small cracks are observed in NFM while no obvious crack could be observed in NFMMT. The formation of cracks of NFM after 100 cycles may be due to the large volume change during the Na$^+$ extraction/insertion process. TEM studies further show that NFM can easily form surface distortion and cracking, while NFMMT shows well-maintained layered structures and less cracking at the surface, as shown in Figure S22 (Supporting Information). The results further confirm the structural stability of NFMMT during cycling.

The thermal stability of cathode materials strongly influences the safety of batteries. To study the thermal performance of the two materials, high-temperature in situ XRD was further employed to examine the structural stability of charged NFM and NFMMT cathodes at elevated temperatures. Figure 3c and Figure S23 (Supporting Information) present the in situ XRD patterns of 4.5 V-charged NFM during heating from 30 to 400 °C, while Figure 3d and Figure S24 (Supporting Information) present those of NFMMT. In Figure 3c, the (002) peak located at 1.3° belongs to the layered O2 structure. With the increase of temperature, the (002) peak gradually shifts to lower angles due to the lattice expansion at elevated temperature. When further heating the charged NFM to ≈175 °C, a small peak at a lower angle corresponding to the rock salt structure appears, while the layered (002) peak gradually becomes weaker. The layered (002) peak disappears at ≈320 °C, suggesting the O2-to-rock salt phase transition. The results can also be observed clearly in the enlarged XRD result between 1° to 1.5° (Figure 3c). The correlation coefficient matrix exhibits the relationship of adjacent XRD patterns. Thus, the 2D color-filled correlation coefficient matrix image (Figure S25a, Supporting Information) for NFM is derived from XRD results, further confirming the phase transition between 175 and 320 °C. For NFMMT, the peak located at ≈1.2° belongs to the layered OP4 structure, which exhibits a similar shift to lower angles with the temperature increase (Figure 3d). Compared with that of the charged NFM cathode, the layered (002) peak of the charged NFMMT cathode becomes weak at a higher temperature of 290 °C. More importantly, no new peak appears during the entire heating process. Enlarged XRD result (Figure S24, Supporting Information) and 2D color-filled correlation coefficient matrix image (Figure S25b, Supporting Information) further confirm that the charged NFMMT is quite stable even up to 400 °C.

## 2.4. Metal CRR Activity and Stability

The charge compensation mechanism of NFMMT was studied by synchrotron X-ray absorption spectroscopy. The X-ray absorption near-edge spectroscopy (XANES) K-edge spectra of Mn in Figure S26 (Supporting Information) show two small peaks located at 6539 and 6542 eV, indicating the $MnO_6$ coordination. The enlarged Mn K-edge XANES spectra during the charge process is presented in **Figure 4a**. In the pristine state, the valence of Mn is +3.99 by comparing with the reference $Mn_2O_3$ and $MnO_2$.[50,55] During the charge process, the edges do not exhibit visible shifts, with only slight lineshape changes, suggesting the negligible change of the local environment of $Mn^{4+}$ ions. During the discharge process from 4.5 to 2.5 V (Figure 4b), no obvious edge shift can be observed either, suggesting the maintenance of the $Mn^{4+}$ state in this range. When further discharged to 1.5 V, the Mn K-edge XANES spectrum shifts to the lower energy region, corresponding to the reduction of $Mn^{4+}$. Extended X-ray absorption fine structure (EXAFS) spectra of Mn were further examined as shown in Figure 4c. Two peaks are observed at ≈1.4 and 2.5 Å, corresponding to the Mn—O and Mn—TM bonds, respectively. During the process of charging to 4.5 V and then discharging to 2.5 V, the Mn—O bond length in NFMMT maintains constant to be 1.4 Å with no shift. Nevertheless, further discharging to 1.5 V results in the obvious shift of the Mn—O bond to 1.52 Å, demonstrating the reduction of $Mn^{4+}$ only at low voltages below 2.5 V.

Compared with the relatively inactive Mn, Fe has an active redox reaction across a wide energy range, as demonstrated by the K-edge XANES spectra (Figure S27, Supporting Information). The valence state of Fe is determined to be ≈+2.98 in the pristine NFMMT by comparing with the reference $Fe_2O_3$ and $Fe_3O_4$.[56] Throughout the charge process, the Fe K-edge spectra continuously shift to the higher energy region, corresponding to the oxidation of Fe during Na$^+$ extraction (Figure 4d). During the discharge process above 2.5 V, the edge gradually shifts to the lower energy region, indicating the reduction of Fe during Na$^+$ insertion (Figure 4e). Pre-edge peaks at ≈7112 eV in Fe K-edge profiles in Figure S28 (Supporting Information) are slightly intensified during the charge process, which is attributed to an electric quadrupole transition of a Fe 1s electron to the Fe 3d orbitals and an electric dipole transition of a Fe 1s electron to the hybridized O 2p-Fe 3d orbitals. The broadness and high intensities of the pre-edge peaks indicate the large contribution of the latter transition and the hole formation in the hybridized O 2p orbitals.[57] Note that there is no obvious edge shift except a slight shape change when further discharged from 2.5 to 1.5 V, suggesting no further reduction of Fe takes place in this low-voltage range. As shown in the EXAFS result (Figure 4f), the Fe—O bond length gradually increases from 1.51 Å upon the charge and decreases back upon discharge to 2.5 V. Peaks located at ≈1.1 Å are ascribed to the sidelobe effect.[58,59] Therefore, it is clear that Fe is active in the high voltage range. Similar situations are also observed for Mn and Fe K-edge profiles in the second and even 50th cycles (Figures S29,S30, Supporting Information).

Assessment of XANES over cycling is also derived from the synchrotron ex situ XAS results in Figures S29 and S30 (Supporting Information). According to the change of valence states of Mn, it is calculated that the Mn-induced capacity can retain 89.8%
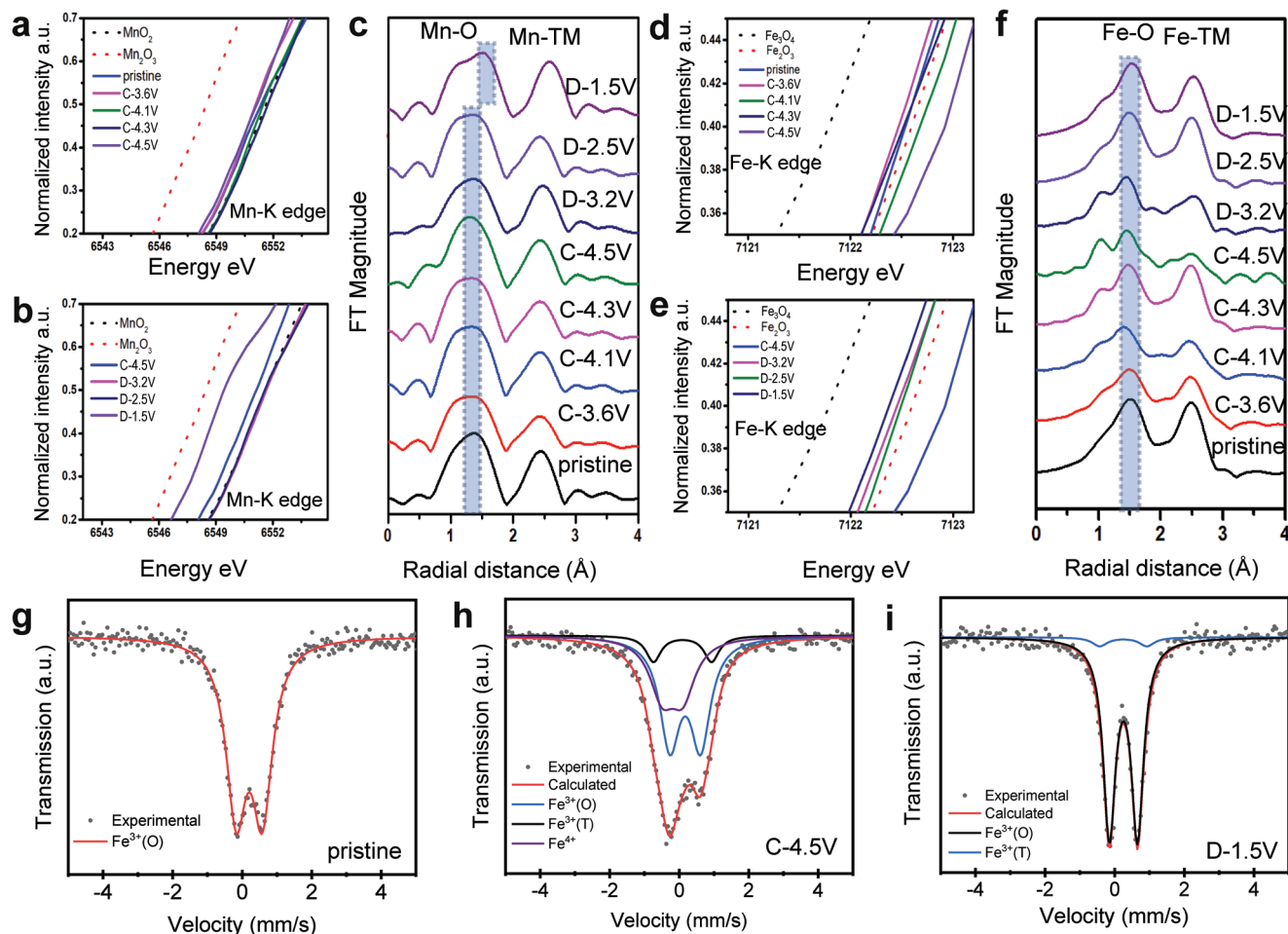
**ADVANCED**
SCIENCE NEWS

www.advancedsciencenews.com

**ADVANCED
MATERIALS**

www.advmat.de

**Figure 4.** XAS and $^{57}$Fe Mössbauer characterizations of NFMMT. a,b) Enlarged XAS Mn K-edge spectra during the initial charge (a) and discharge (b) processes. c) The corresponding Fourier transform results. d, e) Enlarged XAS Fe K-edge spectra during the initial charge (d) and discharge (e) processes. f) The corresponding Fourier transform results. g–i) $^{57}$Fe Mössbauer spectra of NFMMT at pristine (g), fully charged (h), and fully discharged (i) states. D stands for discharge, while C stands for charge, the same below.

in the second cycle and 64.9% in the 50th cycle. The continuous loss of Mn-induced capacity may be attributed to the Jahn–Teller effect and Mn dissolution upon cycling. Similarly, it is calculated that the Fe-induced capacity can retain 67.2% in the second cycle and 65.8% in the 50th cycle. Obviously, the loss of Fe-induced capacity mainly occurs during the first cycle, which may be related with the migration of Fe ions in the first cycle.[37–39]

The migration of TM might trigger the activation of lattice oxygen in layered oxides.[60,61] Fe migration is also recognized as a degradation mechanism for Fe-rich Li and Na compounds.[35,40,61–63] Ex situ $^{57}$Fe Mössbauer spectra on NFMMT at pristine, fully charged (4.5 V), and fully discharged (1.5 V) states in the first cycle were further acquired, as shown in Figure 4g–i. The isomer shift (IS), quadrupole splitting, and relative concentrations of $Fe^{3+}/Fe^{4+}$ ions are obtained by peak fitting (Table S6, Supporting Information).[60,61,64] Figure 4g shows that the spectrum of pristine NFMMT is composed of a single sharp doublet, in good agreement with that of $Fe^{3+}$ in the $FeO_6$ octahedral environment ($Fe^{3+}$(O)). At the fully charged state (Figure 4h), the spectrum becomes asymmetric in the doublet, which could be fitted into three components including $Fe^{3+}$(O),

$Fe^{3+}$(T) ($Fe^{3+}$ in the $FeO_4$ tetrahedral environment), and $Fe^{4+}O_6$. The area percentages of $Fe^{3+}$(O), $Fe^{3+}$(T), and $Fe^{4+}O_6$ are 55.0%, 10.1%, and 34.9%, respectively. The formation of $Fe^{4+}O_6$ demonstrates the $Fe^{3+}/Fe^{4+}$ redox of NFMMT at high voltage, in agreement with the XAS Fe K-edge spectra in Figure 4d–f. The formation of $Fe^{3+}$(T) indicates that a small portion of $Fe^{3+}$ ions could migrate during the charge process. At the fully discharge state, Fe in NFMMT returns to $Fe^{3+}$(O) and $Fe^{3+}$(T), with area percentages of 94.7% and 5.3%, respectively, suggesting the Fe migration in the first cycle is partially reversible. The above results indicate that $Fe^{3+}$ in NFMMT would undergo oxidation to $Fe^{4+}$ and Fe migration upon charge. The Fe migration process may favor the formation of unpaired electrons in the O 2p orbital, which triggers the oxygen anionic redox reaction for NFMMT.

## 2.5. Oxygen ARR Activity and Stability

Considering the molar ratio of Fe (0.3) in the NFMMT formula, Fe can contribute a theoretical specific capacity of ≈80 mAh g$^{-1}$

**ADVANCED
SCIENCE NEWS**

www.advancedsciencenews.com

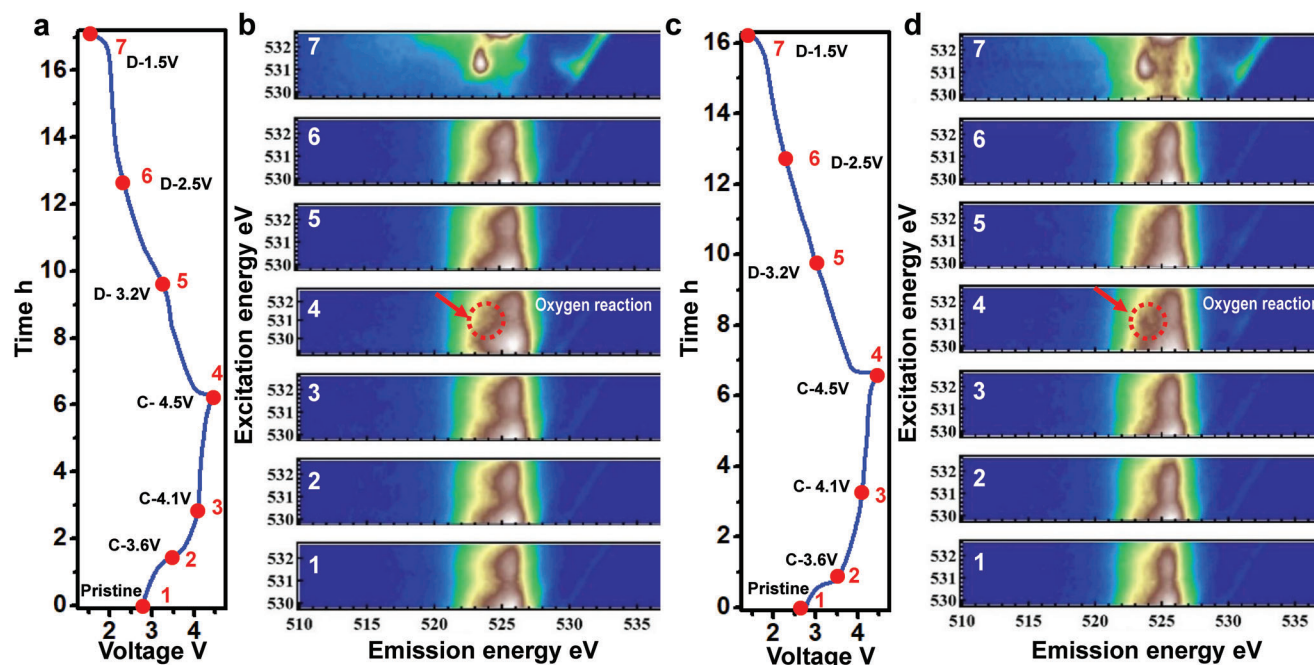**ADVANCED
MATERIALS**

www.advmat.de

**Figure 5.** mRIXS studies of NFM and NFMMT. a,b) Initial Charge and discharge profiles (a) and corresponding mRIXS image of O K-edge (b) of NFM. c,d) Initial Charge and discharge profiles (c) and corresponding mRIXS image of O K-edge (d) of NFMMT.

based on its redox reaction. Therefore, ARR becomes necessary to achieve the tested high capacity ($\approx 200$ mAh g$^{-1}$). It thus becomes important to characterize the ARR activities, especially at high voltages. As clarified recently, the conventional O K-edge absorption spectroscopy is interfered by the transition metal characters, and its variation is misleading in studying ARR states.[43] We therefore employed the high-efficiency O K-edge mapping of resonant inelastic X-ray scattering (mRIXS), which has been established as a powerful probe to scrutinize the lattice ARR activities in various cathodes of NIBs/LIBs.[13,19,20] It has been found that a dedicated mRIXS feature at $\approx 531$ eV excitation and 523.7 eV emission energies can be used to fingerprint the lattice ARR, and its intensity variation could be tracked to monitor the reversibility and decay of the reaction.[19,20] **Figure 5** presents the initial charge/discharge process (Figure 5a,c) and the continuous evolutions of the mRIXS maps (Figure 5b,d) for both materials, in which the intensities around the characteristic energy range of ARR get enhanced at high voltages (red circles in Figure 5b,d). This could also be directly seen from the RIXS cut profiles at 531 eV excitation energy (Figure S31c,f, Supporting Information), which show clearly enhanced intensities $\approx 523.7$ eV at high voltages compared with the pristine/discharged NFM or NFMMT. Upon discharge, the signals of the lattice oxidized oxygen in both materials disappear, indicating a reversible ARR for both. When the system is discharged to 1.5 V, the typical TM—O hybridization feature $\approx 525$ eV emission energy has been significantly enhanced, indicating the signals are not from the layered oxide but from a surface layer, which has been often found in Li-rich compounds.[49] At this time, details on cathode–electrolyte-interphase remain elusive and a grand challenge topic in the battery field, which is not a topic of this work, but we note that the patterns observed here are close to surface peroxide species.[65]

Although this takes place only at the deeply discharged 1.5 V state, the surface reaction typically affects the cycling stability, which also indicates that future improvement of the material through surface coating may be possible. Figure S31 (Supporting Information) presents a comparative study of the ARR activities in NFM (Figure S31a,b, Supporting Information) and NFMMT (Figure S31d,e, Supporting Information) at representative electrochemical states. It can be clearly seen that the charge of initial NFM or NFMMT to 4.5 V led to the change of the mRIXS maps and the appearance of the ARR features, as indicated by the red arrows and red circles. It is important to emphasize that mRIXS results reveal that the ARR is much stronger in NFMMT compared with NFM, which directly suggests that ARR gets enhanced in the Mg/Ti co-doped system. The Mg dopant is highly ionic and generates an O environment similar to that in the alkali-rich configuration, which could promote the activation of ARR.[20,23] The above mRIXS result shows that NFMMT has a more noticeable ARR than NFM, implying the important role of Mg dopant on the activation of lattice oxygen. On the other hand, as suggested by the above ex situ $^{57}$Fe Mössbauer result, the Fe migration may also promote the formation of unpaired electrons to trigger the oxygen ARR.

Differential electrochemical mass spectrometry (DEMS) measurements for both NFM and NFMMT in the initial three cycles were conducted to analyze the gas releases. As shown in Figures S32,S33 (Supporting Information), both NFM and NFMMT release $CO_2$ during the Na$^+$ extraction process, which may come from the decomposition of carbonates or the reactions between oxidative species and electrolytes.[30] In general, although no obvious released $O_2$ is observed for both NFM and NFMMT during the whole cycle process, it can be clearly seen that NFMMT exhibits a much smaller $CO_2$ release, indicating

**ADVANCED
SCIENCE NEWS**

www.advancedsciencenews.com
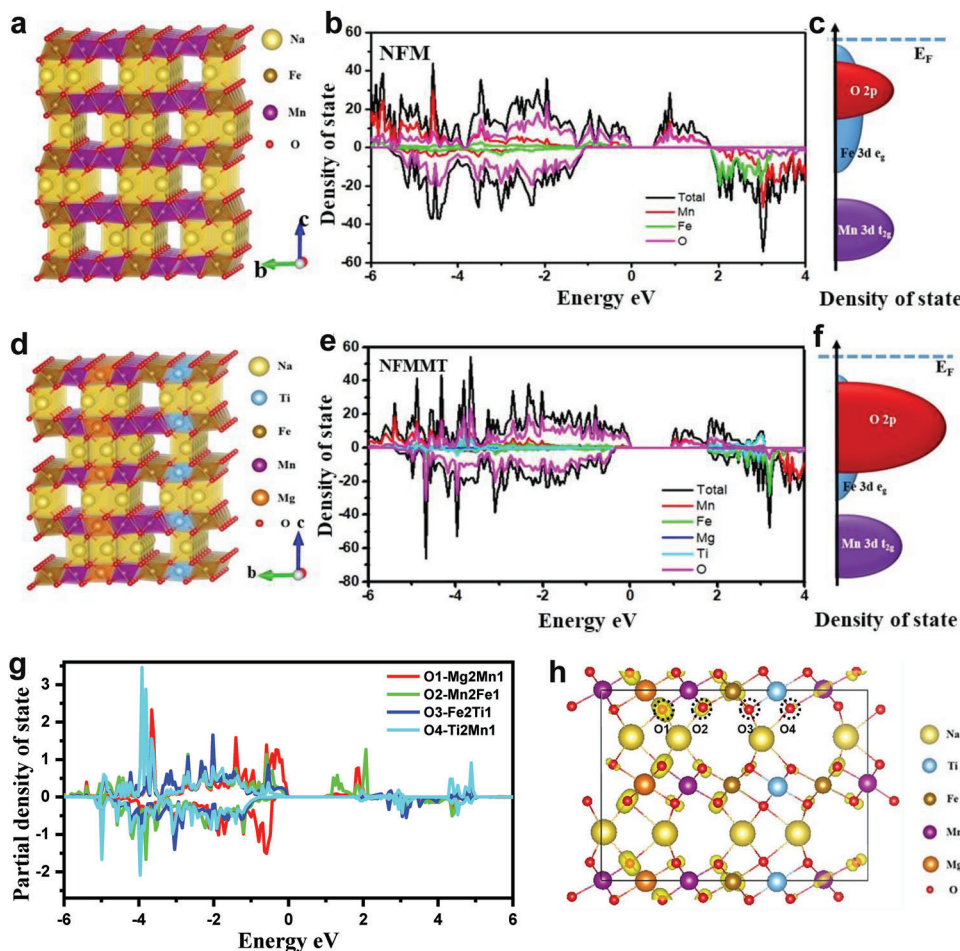
**ADVANCED
MATERIALS**

www.advmat.de

**Figure 6.** a) The model of NFM for the first principles calculations. b) Density of state and c) schematic illustrating the energy versus density of states in NFM. d) Model of NFMMT for the first principles calculations. e) Density of state and f) schematic illustrating the energy versus density of states in NFMMT. g) PDOS of differently coordinated O in NFMMT. h) Highest occupied state charge density for NFMMT (−1–0 eV energy range).

better interfacial stability and better oxygen redox stability by Mg/Ti co-doping.

Theoretical calculations were also conducted for both NFM and NFMMT to understand the mechanism of enhanced ARR in NFMMT (**Figure 6**). The models of NFM and NFMMT for the first principles calculations are shown in Figure 6a,d, respectively. The calculated results of the density of state are shown in Figure 6b,e, respectively. Obviously, enhanced oxygen redox activity can be observed in NFMMT (Figure 6f) when compared with NFM (Figure 6c). The quantitative analysis of the density of the state of NFM and NFMMT was further proceeded. The proportions of O 2p and TM 3d electrons near the Fermi energy level in the energy range of −1–0 eV for NFM and NFMMT were further quantified. The proportions of O 2p and TM 3d of NFM are 71% and 29%, while the proportions of O 2p and TM 3d of NFM are 84% and 16%, respectively. To further understand the effect of Mg and Ti on the charge states of O, the partial density of the state with different O coordination configurations has been further plotted (Figure 6g). Compared to those in other configurations, the O 2p electrons in O1-Mg2Mn1 coordinated with two Mg and one Mn are obviously clustered near

the Fermi energy level and have higher reactivity. This could be ascribed to that the hybridization between Mg and O is weak and the weakly hybridized O 2p electrons due to the Na─O─Mg configuration are reactive during the charge process. In addition, a comparison of the highest occupied state (HOS) charge density plots in the −1–0 eV energy range reveals that most of the high-energy O 2p electrons are clustered around O1-Mg2Mn1 (Figure 6h). When half of Na$^+$ is extracted, NFMMT produces distinct unoccupied states of O above the Fermi energy level, while NFM is dominated by TM transitions (Figure S34a,b, Supporting Information). Moreover, the Bader charge changes of TM and O in NFM are 0.086 and 0.108, while those of TM and O in NFMMT are 0.065 and 0.121, respectively. In addition, the HOS charge density results of the desodiation state indicate that the high-energy electrons of NFM are clustered around Fe, and the subsequent charge compensation is still dominated by Fe (Figure S34c,d, Supporting Information). In contrast, the high-energy electrons of NFMMT are clustered around O, and a more pronounced anionic reaction will occur in the deep desodiation stage. The results suggest that the co-doping of Mg and Ti will enhance the oxygen reaction in NFMMT while eliminating other
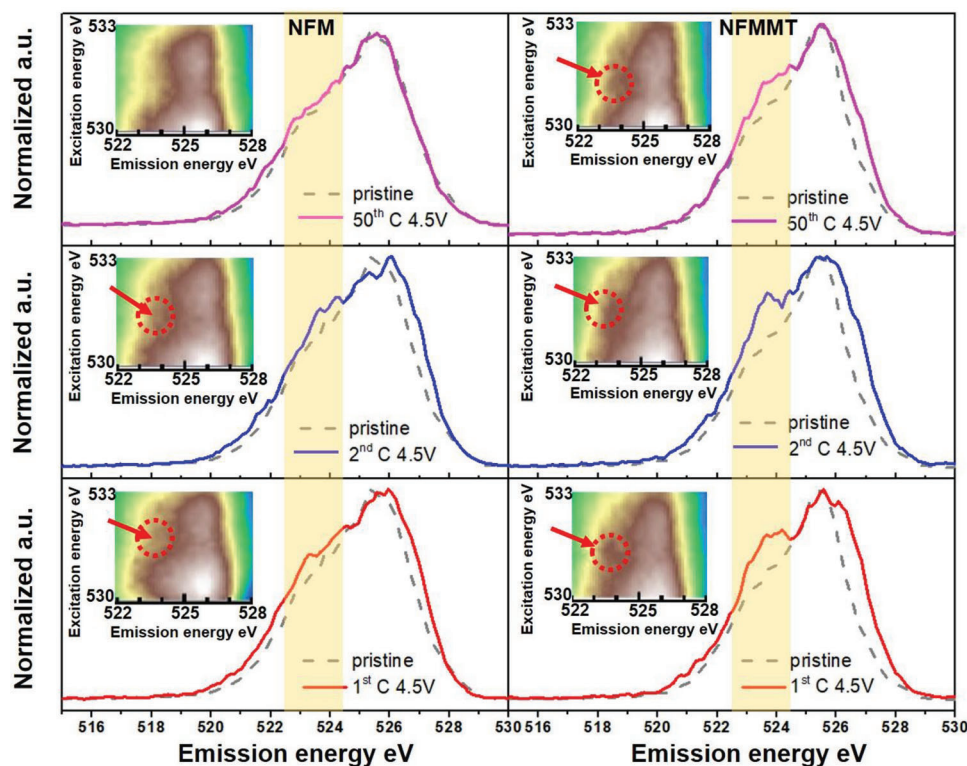
**Figure 7.** Stability of Oxygen Anionic Redox Reaction. The RIXS cut peaks of NFM (left) and NFMMT (right) at the first, second, and 50th charged states. The inset images show the corresponding mRIXS results.

detrimental oxygen activities such as oxygen gas release and surface reactions of radical oxygen, which is consistent with the mRIXS results.

As discussed above, the co-doping of Mg and Ti can also lead to a more stable structure, which could be ascribed to the Ti-induced weakening of Jahn–Teller effect and Mn dissolution, and also the strong Mg—O bonds and Mg migration. To further understand the effect of Mg/Ti co-doping on the structure stability, we have examined the formation energies of typical O vacancies in the two materials. As shown in Figure S35 (Supporting Information), the formation energies of two typical kinds of O vacancies in NFMMT are larger than that of NFM. Clearly, co-doping makes the lattice O more difficult to escape by forming O vacancy, thereby stabilizing the TMs dissolution and the layered framework.

Oxygen ARR offers high energy to cathode materials, however, often suffers from fast decay upon cycling.[14,24,26] It is thus important to evaluate the stability of ARR in the two materials. Figure 7 shows the RIXS results of the fully charged states of the two materials in the first, second, and 50th cycles. The individual RIXS cuts at 531 eV excitation energy display that, compared with that of NFM, the stronger ARR sustains a much more stable cycling in NFMMT. The inset mRIXS maps show the same result. For NFM, the ARR feature could still be observed at the second charged state, but no obvious feature could be seen at the 50th charged state, indicating ARR decays within tens of cycles in the NFM system. By contrast, for NFMMT, the ARR feature located at 523.7 eV emission energy can be still clearly seen at the second and 50th charged states. This is also consistent

with the electrochemical performance of the NFMMT electrode which displays both higher capacity and better cycling stability (Figure 2).

ARR quantification was also conducted based on our previously established method. The variations of the fingerprint feature intensity in O-K mRIXS were carefully quantified upon cycling, as shown in **Figure 7**. Specifically, we first normalized all the spectra to the broad hybridization feature (Figure S36, Supporting Information), then calculated the intensity differences between the cycled electrodes and the pristine sample to obtain the oxidized oxygen peak variation upon cycling up to 50 cycles (Table S7, Supporting Information). As indicated by these quantifications, the ARRs of NFMMT and NFM show a decay of ≈34% (0.18 to 0.12) and ≈67% (0.09 to 0.03) after 50 cycles, respectively. The second cycle data show negligible changes based on such a spectroscopic estimation, indicating the decay does not take place suddenly as in Li-rich materials. Although this is only a rough estimation based on spectroscopic results, the big difference between NTMMT (66% retained after 50 cycles) and NFM (33% retained after 50 cycles) here implies that the ARR reversibility is indeed improved in NFMMT.

We note that, at this time, there is no technique that could provide absolute quantification of the ARR charge transfer number, so we could only deduct the relative changes of the oxidized oxygen feature instead of the absolute value of the redox capacity. Nevertheless, combined with the TM analysis above, we can deliver an overall picture. Another conclusion through the quantification here is that NFMMT offers both stronger reactions and better reversibility of ARR than those of NFM. Compared

**ADVANCED
SCIENCE NEWS**

www.advancedsciencenews.com

**ADVANCED
MATERIALS**

www.advmat.de

with NFM, the improved capacity/voltage retention of NFMMT can be ascribed to the improved stabilities of the mixed and correlated CRR and ARR activities. In addition, the doped Mg and Ti may also play a role for the stabilization of the ARR process.[23,26]

## 3. Conclusion

In summary, this work designed a high-capacity and earth-abundant layered oxide cathode for advanced NIBs. The stable cathode material NFMMT (P2 $Na_{0.67}Fe_{0.3}Mn_{0.5}Mg_{0.1}Ti_{0.1}O_2$), shows a high capacity of >200 mAh $g^{-1}$ at 20 mA $g^{-1}$ and good cycling stability even when charging/discharging between 1.5–4.5 V (vs $Na^+/Na$). Compared with the pristine NFM ($Na_{0.67}Fe_{0.4}Mn_{0.6}O_2$) cathode, NFMMT significantly enhanced electrochemical, structural, and thermal stabilities, as demonstrated by the simpler electrochemical phase transition and less phase change of the fully charged NFMMT during heating, respectively. More importantly, NFMMT displays stronger ARR activities than NFM upon cycling, surprisingly, with clear improvements on stability. The stabilized ARR activities in NFMMT demonstrate that oxygen redox activities can be enhanced and stabilized synchronously. Our present findings provide useful insights into the optimization of dopants, for instance, multi-cations or high-entropy dopants, to improve the cycling stability of Fe/Mn-based layered oxide cathodes.

## 4. Experimental Section

*Material Synthesis*: P2-NFM and P2-MFMMT were synthesized by a traditional solid-state reaction. For NFM, stoichiometric amounts of $Na_2CO_3$ (Sinopharm Chemical Reagent Co., Ltd.), $MnO_2$ (Sinopharm Chemical Reagent Co., Ltd.), and FeO (Sinopharm Chemical Reagent Co., Ltd.) were thoroughly mixed by ball milling overnight at 300 rpm ($ZrO_2$ balls with a ball-to-powder ratio of 8:1) using a FRITSCH P7 8000D DUAL MIXER/MILL. The obtained mixture was dried at 100 °C, calcined at 700 °C for 5 h, and then cooled in air (muffle furnace). After that, the mixture was pressed into pellets (300 mg for each, prepared at 10 MPa), which were calcined at 950 °C in $O_2$ for 15 h (tube furnace). The ramp rate was 5 °C min$^{-1}$. After cooling to room temperature, the obtained NFM was collected in an argon glove box. P2-NFMMT was synthesized under the same conditions with stoichiometric amounts of $Na_2CO_3$ (Sinopharm Chemical Reagent Co., Ltd.), $MnO_2$ (Sinopharm Chemical Reagent Co., Ltd.), FeO (Sinopharm Chemical Reagent Co., Ltd.), $TiO_2$ (Sinopharm Chemical Reagent Co., Ltd.), and MgO (Sinopharm Chemical Reagent Co., Ltd.). P2-NFMM and P2-NFMT were synthesized under the same conditions as that of P2-NFMMT except without $TiO_2$ or MgO, respectively.

*Electrochemical Measurements*: Cathode active materials (NFM, NFMM, NFMT, or NFMMT), carbon black (MREDA), and polyvinylidenefluoride (PVDF, SOLVAY SOLEF PVDF 5130) with a weight ratio of 75:15:10 were used to prepare the electrode. PVDF was first added into N-methylpyrrolidone (NMP) to prepare a uniform suspension. Then, the cathode materials and carbon black were added into the suspension, which were further mixed by a mixing machine. The slurry was then coated on Al foil with an areal density of 3.68–4.94 mg cm$^{-2}$ and dried at 80 °C in a vacuum oven for 12 h. The obtained electrodes (12 mm in diameter) were assembled in CR2032 coin-type cells under a pressure of 50 MPa in an argon-filled glove box, using ≈150 µL NaClO$_4$ electrolyte (1 mol L$^{-1}$ NaClO$_4$ dissolved in propylene carbonate (PC) (Tomiyama Pure Chemical Industries, the same below), with 2 vol.% fluorinated ethylene carbonate additive). The water content of the non-aqueous electrolyte solution was 20–40 ppm. The Na metal (MACKLIN, AR, ≥99.5%) counter electrode

was cut by knife in the Ar-filled glove box to remove the oxide layer and adjust the content, then the clean Na metal was pressed into disc with a diameter of 12 mm and a thickness of ≈500 µm. The Whatman GF/A glass fiber was used as the separator, which has a thickness of 260 µm, a pore size of ≈1.6 µm, and a diameter of 16 mm. Electrochemical performance was tested by LAND CT2001A battery test system (Wuhan, PR China) in environmental chambers at a constant temperature of 25 ± 1 °C.

CR2032 coin-type cells (MTI) with 2 mm holes were used for in situ XRD measurement. In order to avoid exposure of cathode material to air, holes were sealed with plastic Kapton tape (Sigma-Aldrich), which had no XRD peak. Other steps were the same as the conventional coin cell assembling process, which were carried out at 50 MPa in an argon-filled glove box.

*Material Characterizations*: To test the air stability, 1.5 g NFM and 1.5 g NFMMT powder materials were taken out from the glove box and exposed to air for a month, and then characterized by XRD (Bruker, advanced D8). The step was 0.02° and the rate was two seconds per step.

For the ICP test, both NFM and NFMMT powder materials with a weight of 10 mg were dissolved in 20 mL chloroazotic acid, which was prepared by HCl (Sinopharm Chemical Reagent Co., Ltd.) and HNO$_3$ (Sinopharm Chemical Reagent Co., Ltd.). Then, 1 mL of each solution was diluted by DI water to 100 mL for the ICP (OPTIMA7000DV) test.

XPS was used to identify the average valences of Mg and Ti after the activation of NFMMT in NIBs, which was performed by XPS (PHI Quantera II) with a monochromatic Al Kα X-ray source.

In situ DEMS was carried out to study the different gases generated during cell cycling. The equipment consisted of a quadrupole mass spectrometer (Thermo Fischer) equipped with a turbomolecular pump and mass-flow controllers (Bronkhorst). The NIBs with gas inlet and outlet ports for the in situ DEMS test were assembled in a mold with either NFM or NFMMT (10 mg) and 0.3 mL NaClO$_4$ electrolyte. The NIBs were tested by an electrochemical workstation (Chenhua, CHI1400) at 20 mA $g^{-1}$ for three cycles to synchronously proceed the in situ DEMS analysis.

Ex situ and in situ XRD patterns were collected at Sector 11-ID-C of the Advanced Photon Source (APS) in Argonne National Laboratory. The X-ray preset wavelength was 0.117418 Å. The data was exchanged by Fit 2D software with 4000 points from 1° to 8° using CeO$_2$ as a standard reference material. Rietveld refinement was accomplished using the commercialized Topas software. High-temperature in situ XRD for both NFM and NFMMT were collected at Sector 11-ID-C of APS, with a ramp rate of 5 °C min$^{-1}$ from 30 to 400 °C. Both materials were assembled in CR2032 coin-type cells under 50 MPa in an argon-filled glove box, using 150 µL NaClO$_4$ electrolyte. Then the cells were charged to 4.5 V and maintained at the constant voltage for 20 h. After that, the charged cells were disassembled in an Ar glove box. The cathode materials were washed with dimethyl carbonate (DMC) to remove the remaining electrolyte and then collected from the current collector. Subsequently, the cathode materials were transferred to a sealed crucible for high-temperature XRD test, in which the crucible was sealed by plastic Kapton tape.

The atomic-resolution imaging and EDX mapping of cathode materials were performed on a double aberration-corrected JEOL-ARM200CF microscope with a cold field emission gun operating at 200 KV. The convergent semi-angle of 23 mrad was adopted for high-angle annular dark field scanning transmission electron microscopy imaging (HAADF-STEM) and annular bright field STEM imaging (ABF-STEM) with the corresponding collection semi-angle of 90–370 and 11–23 mrad, respectively. To improve the signal-to-noise ratio, atomically resolved STEM images were subjected to the average background subtraction filtering implemented in DigitalMicrograph software.

XANES experiments on the Mn K-edge and Fe K-edge of both NFM and NFMMT were carried out in the transmission mode at Beamline 20-BM of the APS. O K-edge mRIXS was measured in the high-efficiency iRIXS end station at Beamline 8.0.1 of Advanced Light Source, Lawrence Berkeley National Laboratory. The energy resolution of the incident (excitation) X-ray beam was ≈0.2 eV. RIXS cut at 531 eV excitation energy was extracted from the corresponding mRIXS. All the samples were prepared in the argon-filled glove box. To avoid any air exposure, samples were sealed in a homemade suitcase[66] and transferred into the experimental vacuum chamber.

The $^{57}$Fe Mössbauer spectroscopy characterization of NFMMT was carried out on an SEE Co W304 Mössbauer spectrometer, using a $^{57}$Co/Rh source in transmission geometry. The data were fitted with the MossWinn 4.0 software.

*DFT Calculations*: The density functional theory (DFT) calculations were performed using the pseudopotentials based on projector augmented wave and the Perdew–Burke–Ernzerh implemented in the Vienna ab initio package. The strong correlation effect of Mn, Fe, and Ti was modified by DFT with Hubbard U correction. The Brillouin zone was adopted with a $3 \times 2 \times 2$ Γ-centered k-mesh, and the plane-wave basis was cut off by 520 eV. All structures were relaxed, and the total energy converged was set to be $10^{-5}$ eV. For a more accurate band gap, the U values were set to Ti = 2.5, Fe = 4.9, and Mn = 4.9 eV. O-vacancy formation energy ($\Delta E$) is obtained by the energy difference between the O-deficient model and the pristine model (Equation (1)), where $x$ is the amount of O removed from the lattice:

$$\Delta E = \frac{E(O - deficient) + 0.5xE(O_2) - E(pristine)}{0.5x} \tag{1}$$

## Supporting Information

Supporting Information is available from the Wiley Online Library or from the author.

## Acknowledgements

## Conflict of Interest

The authors declare no conflict of interest.

## Data Availability Statement

The data that support the findings of this study are available from the corresponding author upon reasonable request.

## Keywords

[1] H. S. Hirsh, Y. X. Li, D. H. S. Tan, M. H. Zhang, E. Y. Zhao, Y. S. Meng, *Adv. Energy Mater.* **2020**, *10*, 2001274.

[2] Z. Zhu, T. Jiang, M. Ali, Y. Meng, Y. Jin, Y. Cui, W. Chen, *Chem. Rev.* **2022**, *122*, 16610.

[3] N. Yabuuchi, K. Kubota, M. Dahbi, S. Komaba, *Chem. Rev.* **2014**, *114*, 11636.

[4] X. Liu, B. W. Xiao, A. Daali, X. W. Zhou, Z. Yu, X. Li, Y. Z. Liu, L. Yin, Z. Z. Yang, C. Zhao, L. K. Zhu, Y. Ren, L. Cheng, S. Ahmed, Z. H. Chen, X. L. Li, G. L. Xu, K. Amine, *ACS Energy Lett.* **2021**, *6*, 547.

[5] K. Chayambuka, G. Mulder, D. L. Danilov, P. H. L. Notten, *Adv. Energy Mater.* **2020**, *10*, 2001310.

[6] G. L. Xu, R. Amine, Y. F. Xu, J. Z. Liu, J. Gim, T. Y. Ma, Y. Ren, C. J. Sun, Y. Z. Liu, X. Y. Zhang, S. M. Heald, A. Solhy, I. Saadoune, W. L. Mattis, S. G. Sun, Z. H. Chen, K. Amine, *Energy Environ. Sci.* **2017**, *10*, 1677.

[7] S. H. Guo, P. Liu, H. J. Yu, Y. B. Zhu, M. W. Chen, M. Ishida, H. S. Zhou, *Angew. Chem., Int. Ed.* **2015**, *54*, 5894.

[8] J. H. Song, K. Wang, J. M. Zheng, M. H. Engelhard, B. W. Xiao, E. Y. Hu, Z. H. Zhu, C. M. Wang, M. L. Sui, Y. H. Lin, D. Reed, V. L. Sprenkle, P. F. Yan, X. L. Li, *ACS Energy Lett.* **2020**, *5*, 1718.

[9] Q. Wang, S. Mariyappan, G. Rousse, A. V. Morozov, B. Porcheron, R. Dedryvère, J. Wu, W. Yang, L. Zhang, M. Chakir, *Nat. Mater.* **2021**, *20*, 353.

[10] K. Zhang, D. Kim, Z. Hu, M. Park, G. Noh, Y. Yang, J. Zhang, V. W.-h. Lau, S.-L. Chou, M. Cho, *Nat. Commun.* **2019**, *10*, 5203.

[11] R. A. House, U. Maitra, M. A. Pérez-Osorio, J. G. Lozano, L. Jin, J. W. Somerville, L. C. Duda, A. Nag, A. Walters, K.-J. Zhou, *Nature* **2020**, *577*, 502.

[12] A. Gao, Q. Zhang, X. Li, T. Shang, Z. Tang, X. Lu, Y. Luo, J. Ding, W. H. Kan, H. Chen, *Nat. Sustainability* **2022**, *5*, 214.

[13] X. H. Rong, J. Liu, E. Y. Hu, Y. J. Liu, Y. Wang, J. P. Wu, X. Q. Yu, K. Page, Y. S. Hu, W. L. Yang, H. Li, X. Q. Yang, L. Q. Chen, X. J. Huang, *Joule* **2018**, *2*, 125.

[14] D. Kim, M. Cho, K. Cho, *Adv. Mater.* **2017**, *29*, 1701788.

[15] G. H. Lee, J. P. Wu, D. Kim, K. Cho, M. Cho, W. L. Yang, Y. M. Kang, *Angew. Chem., Int. Ed.* **2020**, *59*, 8681.

[16] M. M. Rahman, F. Lin, *Matter* **2021**, *4*, 490.

[17] C. Li, F. Geng, B. Hu, *Mater. Today Energy* **2020**, *17*, 25.

[18] D. H. Seo, J. Lee, A. Urban, R. Malik, S. Kang, G. Ceder, *Nat. Chem.* **2016**, *8*, 692.

[19] K. H. Dai, J. P. Wu, Z. Q. Zhuo, Q. H. Li, S. Sallis, J. Mao, G. Ai, C. H. Sun, Z. Y. Li, W. E. Gent, W. C. Chueh, Y. D. Chuang, R. Zeng, Z. X. Shen, F. Pan, S. S. Yan, L. F. J. Piper, Z. Hussain, G. Liu, W. L. Yang, *Joule* **2019**, *3*, 518.

[20] K. H. Dai, J. Mao, Z. Q. Zhuo, Y. Feng, W. F. Mao, G. Ai, F. Pan, Y. D. Chuang, G. Liu, W. L. Yang, *Nano Energy* **2020**, *74*, 104831.

[21] Q. Li, Y. Qiao, S. H. Guo, K. Z. Jiang, Q. H. Li, J. P. Wu, H. S. Zhou, *Joule* **2018**, *2*, 1134.

[22] C. Li, C. Zhao, B. Hu, W. Tong, M. Shen, B. W. Hu, *Chem. Mater.* **2020**, *32*, 1054.

[23] U. Maitra, R. A. House, J. Somerville, N. Tapia-Ruiz, J. G. Lozano, N. Guerrini, R. Hao, K. Luo, L. Y. Jin, M. A. Perez-Osorio, F. Massel, D. M. Pickup, S. Ramos, X. Y. Lu, D. E. McNally, A. V. Chadwick, F. Giustino, T. Schmitt, L. C. Duda, M. R. Roberts, P. G. Bruce, *Nat. Chem.* **2018**, *10*, 288.

[24] Q. Wang, S. Mariyappan, G. Rousse, A. V. Morozov, B. Porcheron, R. Dedryvere, J. P. Wu, W. L. Yang, L. T. Zhang, M. Chakir, M. Avdeev, M. Deschamps, Y. S. Yu, J. Cabana, M. L. Doublet, A. M. Abakumov, J. M. Tarascon, *Nat. Mater.* **2021**, *20*, 353.

[25] X. Y. Zhang, Y. Qiao, S. H. Guo, K. Z. Jiang, S. Xu, H. Xu, P. Wang, P. He, H. S. Zhou, *Adv. Mater.* **2019**, *31*, 1807770.

[26] X. H. Rong, E. Y. Hu, Y. X. Lu, F. Q. Meng, C. L. Zhao, X. L. Wang, Q. H. Zhang, X. Q. Yu, L. Gu, Y. S. Hu, H. Li, X. J. Huang, X. Q. Yang, C. Delmas, L. Q. Chen, *Joule* **2019**, *3*, 503.

[27] A. Konarov, H. J. Kim, J. H. Jo, N. Voronina, Y. S. Lee, Z. Bakenov, J. Kim, S. T. Myung, *Adv. Energy Mater.* **2020**, *10*, 2001111.

[28] X. Cao, H. F. Li, Y. Qiao, X. Li, M. Jia, J. Cabana, H. S. Zhou, *Adv. Energy Mater.* **2020**, *10*, 1903785.

[29] K. Du, J. Y. Zhu, G. R. Hu, H. C. Gao, Y. T. Li, J. B. Goodenough, *Energy Environ. Sci.* **2016**, *9*, 2575.

[30] X. Cao, X. Li, Y. Qiao, M. Jia, F. L. Qiu, Y. B. He, P. He, H. S. Zhou, *ACS Energy Lett.* **2019**, *4*, 2409.

[31] L. Li, H. B. Wang, W. Z. Han, H. Guo, A. Hoser, Y. J. Chai, X. F. Liu, *J. Electrochem. Soc.* **2018**, *165*, A3854.

[32] C. L. Zhao, Z. P. Yao, J. L. Wang, Y. X. Lu, X. D. Bai, A. Aspuru-Guzik, L. Q. Chen, Y. S. Hu, *Chem* **2019**, *5*, 2913.

[33] H. J. Kim, A. Konarov, J. H. Jo, J. U. Choi, K. Ihm, H. K. Lee, J. Kim, S. T. Myung, *Adv. Energy Mater.* **2019**, *9*, 1901181.

[34] E. Talaie, S. Y. Kim, N. Chen, L. F. Nazar, *Chem. Mater.* **2017**, *29*, 6684.

[35] X. Wang, Q. Zhang, C. Zhao, H. Li, B. Zhang, G. Zeng, Y. Tang, Z. Huang, I. Hwang, H. Zhang, S. Zhou, Y. Qiu, Y. Xiao, J. Cabana, C.-J. Sun, K. Amine, Y. Sun, Q. Wang, G.-L. Xu, L. Gu, Y. Qiao, S.-G. Sun, *Nat. Energy* **2024**, *9*, 184.

[36] N. Yabuuchi, M. Kajiyama, J. Iwatate, H. Nishikawa, S. Hitomi, R. Okuyama, R. Usui, Y. Yamada, S. Komaba, *Nat. Mater.* **2012**, *11*, 512.

[37] D. Susanto, M. K. Cho, G. Ali, J.-Y. Kim, H. J. Chang, H.-S. Kim, K.-W. Nam, K. Y. Chung, *Chem. Mater.* **2019**, *31*, 3644.

[38] E. Lee, D. E. Brown, E. E. Alp, Y. Ren, J. Lu, J.-J. Woo, C. S. Johnson, *Chem. Mater.* **2015**, *27*, 6755.

[39] E. Talaie, V. Duffort, H. L. Smith, B. Fultz, L. F. Nazar, *Energy Environ. Sci.* **2015**, *8*, 2512.

[40] E. Boivin, R. A. House, J. J. Marie, P. G. Bruce, *Adv. Energy Mater.* **2022**, *12*, 2200702.

[41] H. Y. Asl, A. Manthiram, *Science* **2020**, *369*, 140.

[42] Y. Y. Xie, G. L. Xu, H. Y. Che, H. Wang, K. Yang, X. R. Yang, F. M. Guo, Y. Ren, Z. H. Chen, K. Amine, Z. F. Ma, *Chem. Mater.* **2018**, *30*, 4909.

[43] Y. H. Liu, X. Fang, A. Y. Zhang, C. F. Shen, Q. Z. Liu, H. A. Enaya, C. W. Zhou, *Nano Energy* **2016**, *27*, 27.

[44] G. L. Xu, R. Amine, A. Abouimrane, H. Y. Che, M. Dahbi, Z. F. Ma, I. Saadoune, J. Alami, W. L. Mattis, F. Pan, Z. H. Chen, K. Amine, *Adv. Energy Mater.* **2018**, *8*, 1702403.

[45] Y. B. Niu, Y. X. Yin, Y. G. Guo, *Small* **2019**, *15*, 1900233.

[46] S. H. Bo, X. Li, A. J. Toumar, G. Ceder, *Chem. Mater.* **2016**, *28*, 1419.

[47] M. H. Han, E. Gonzalo, N. Sharma, J. M. L. del Amo, M. Armand, M. Avdeev, J. J. S. Garitaonandia, T. Rojo, *Chem. Mater.* **2016**, *28*, 106.

[48] D. Hamani, M. Ati, J. M. Tarascon, P. Rozier, *Electrochem. Commun.* **2011**, *13*, 938.

[49] J. Wu, X. Zhang, S. Zheng, H. Liu, J. Wu, R. Fu, Y. Li, Y. Xiang, R. Liu, W. Zuo, *ACS Appl. Mater. Interfaces* **2020**, *12*, 7277.

[50] D. Pahari, S. Puravankara, *J. Power Sources* **2020**, *455*, 227957.

[51] T. C. Fang, S. H. Guo, K. Z. Jiang, X. Y. Zhang, D. Wang, Y. Z. Feng, X. P. Zhang, P. Wang, P. He, H. S. Zhou, *Small Methods* **2019**, *3*, 1800183.

[52] H. Su, G. C. Guo, Y. Ren, X. Q. Yu, X. Zhang, T. Y. Ma, Y. Lu, Z. H. Zhang, H. Ma, M. L. Sui, H. Li, C. J. Sun, Z. H. Chen, G. L. Xu, R. Z. Wang, K. Amine, H. J. Yu, *Energy Environ. Sci.* **2020**, *13*, 4371.

[53] T. Ungar, *Scr. Mater.* **2004**, *51*, 777.

[54] W. Zuo, X. Liu, J. Qiu, D. Zhang, Z. Xiao, J. Xie, F. Ren, J. Wang, Y. Li, G. F. Ortiz, *Nat. Commun.* **2021**, *12*, 4903.

[55] M. J. Zuba, A. Grenier, Z. Lebens-Higgins, G. J. P. Fajardo, Y. X. Li, Y. Ha, H. Zhou, M. S. Whittingham, W. L. Yang, Y. S. Meng, K. W. Chapman, L. F. J. Piper, *ACS Energy Lett.* **2021**, *6*, 1055.

[56] J. A. van Bokhoven, C. Lamberti, *Coord. Chem. Rev.* **2014**, *277*, 275.

[57] Y. Yoda, K. Kubota, K. Kuroki, S. Suzuki, K. Yamanaka, T. Yaji, S. Amagasa, Y. Yamada, T. Ohta, S. Komaba, *Small* **2020**, *16*, 2006483.

[58] Y. Luo, Z. Zhang, F. Yang, J. Li, Z. Liu, W. Ren, S. Zhang, B. Liu, *Energy Environ. Sci.* **2021**, *14*, 4610.

[59] W. Liu, L. Zhang, X. Liu, X. Liu, X. Yang, S. Miao, W. Wang, A. Wang, T. Zhang, *J. Am. Chem. Soc.* **2017**, *139*, 10790.

[60] X. Gao, L. Fang, H. Wang, S. Lee, H. Liu, S. Zhang, J. Gao, Y. Mei, M. Park, J. Zhang, M. Chen, L. Zhou, W. Deng, G. Zou, H. Hou, Y. M. Kang, X. Ji, *Adv. Funct. Mater.* **2022**, *33*, 2212685.

[61] Y. Niu, Z. Hu, B. Zhang, D. Xiao, H. Mao, L. Zhou, F. Ding, Y. Liu, Y. Yang, J. Xu, W. Yin, N. Zhang, Z. Li, X. Yu, H. Hu, Y. Lu, X. Rong, J. Li, Y. S. Hu, *Adv. Energy Mater.* **2023**, *13*, 2300746.

[62] X. Li, J. Xu, H. Li, H. Zhu, S. Guo, H. Zhou, *Adv. Sci.* **2022**, *9*, 2105280.

[63] X. Gao, L. Fang, H. Wang, S. Lee, H. Liu, S. Zhang, J. Gao, Y. Mei, M. Park, J. Zhang, M. Chen, L. Zhou, W. Deng, G. Zou, H. Hou, Y. M. Kang, X. Ji, *Adv. Funct. Mater.* **2023**, *33*, 2212685.

[64] V. A. Shevchenko, I. S. Glazkova, D. A. Novichkov, I. Skvortsova, A. V. Sobolev, A. M. Abakumov, I. A. Presniakov, O. A. Drozhzhin, E. V. Antipov, *Chem. Mater.* **2023**, *35*, 4015.

[65] Z. Zhuo, C. D. Pemmaraju, J. Vinson, C. Jia, B. Moritz, I. Lee, S. Sallies, Q. Li, J. Wu, K. Dai, Y.-d. Chuang, Z. Hussain, F. Pan, T. P. Devereaux, W. Yang, *J. Phys. Chem. Lett.* **2018**, *9*, 6378.

[66] W. Yang, X. Liu, R. Qiao, P. Olalde-Velasco, J. D. Spear, L. Roseguo, J. X. Pepper, J. D. Denlinger, Z. Hussain, *J. Electron Spectrosc. Relat. Phenom.* **2013**, *190*, 64.